FURTHER EVIDENCE FOR M87'S MASSIVE, DARK HALO

D. FABRICANT AND P. GORENSTEIN
Harvard-Smithsonian Center for Astrophysics
Received 1982 July 6; accepted 1982 October 11

ABSTRACT

X-ray data obtained with the *Einstein Observatory* imaging proportional counter (IPC), supported by data from other detectors aboard the *Einstein Observatory* and previous instruments, allow us to measure rather accurately the distribution of mass surrounding M87 at large radial distances that are inaccessible to optical study. The present work goes beyond a previous paper in that more data are incorporated in the analysis, and a considerable body of calibration data for the IPC's spectral response has been obtained from the observation of other objects. In addition, an essentially complete range of possible temperature profiles for the X-ray emitting gas is considered.

We find that the integral mass-to-light ratio of M87 (in solar units) must increase from 5–15 at 1' (~ 4.4 kpc) to over 180 at 20' (~ 87 kpc). The total mass within 20' of M87 is $1.2–1.9 \times 10^{13}$ $M_{\odot}$, rising to $3–6 \times 10^{13}$ $M_{\odot}$ within 60' of M87. The results are not model dependent and follow from the well-accepted hypothesis that the X-ray emitting gas surrounding M87 is in hydrostatic equilibrium.

Subject headings: galaxies: individual — galaxies: structure

I. INTRODUCTION

Attempts to account for the X-ray emission from M87 observed prior to the launch of the *Einstein Observatory* led to suggestions that M87 is considerably more massive than indicated by conventional optical estimates (Bahcall and Sarazin 1977; Mathews 1978). An analysis of X-ray data acquired with the imaging proportional counter (IPC) on board the *Einstein Observatory* gave this conclusion strong observational support (Fabricant, Lecar, and Gorenstein 1980, hereafter FLG). The purpose of the present paper is to incorporate further X-ray observations and a careful analysis of the experimental errors to further refine the measurement of the mass distribution surrounding M87.

Since the previous paper (FLG) was written, we have analyzed data from three additional IPC pointings adjacent to M87, increasing the accuracy of the X-ray surface brightness profile at large radii. In addition, with a considerably larger data base of observations now available, our understanding of the IPC spectral response has improved markedly. High-resolution spectral data from the two focal plane X-ray spectrometers aboard the *Einstein Observatory*, the solid state spectrometer and the crystal spectrometer, are now available in final form (Lea, Mushotzky, and Holt 1982; Canizares *et al.* 1982). In the regions of spatial overlap, these data provide a valuable confirmation of the spectral information derived from the IPC, which has considerably lower energy resolution. The accuracy of the IPC spectral data and the resultant allowed temperature profiles are key issues since the temperature gradient in the X-ray emit-ting gas affects the the M87 mass derived from the X-ray data.

As before (FLG), our analysis proceeds from the two hypotheses that the X-ray emitting gas is in hydrostatic equilibrium, and that spherical symmetry is a good approximation. The condition of hydrostatic equilibrium has been uniformly adopted as a starting point for the analysis of the X-ray data for several reasons (see Bahcall and Sarazin 1977; Mathews 1978; FLG; Takahara and Takahara 1981; and Binney and Cowie 1981). The most fundamental of these is the fact that we see $\sim 3 \times 10^{12}$ $M_{\odot}$ of gas in total. Since gas at a temperature of 3 keV would expand ~ 100 kpc in 10^8 yr, it must be gravitationally contained if we are not witnessing a transient outflow of huge quantities of gas. In addition, if the gas were freely falling or expanding, one would expect it to show two characteristics: a density profile with radial dependence of the form r^{-2} and a temperature decreasing with increasing radius. The observed radial dependence of the density is considerably shallower, and in the regions very close to M87, at least, the temperature increases with radius.

The X-ray spectral data suggest that the gas surrounding M87 has radiatively cooled in the densest central regions, at radii $\lesssim 3'$. Since the gas cooling time here is $\sim 10^9$ yr, the gas must have been contained against the outflow, which would have taken place on a much shorter time scale. Finally, radiative cooling cannot disrupt hydrostatic equilibrium, because the free-fall time is approximately two orders of magnitude less than the cooling time of the gas (FLG).

Given hydrostatic equilibrium and spherical symmetry, the total mass enclosed within a specified radius may be calculated from the gas temperature and the logarithmic derivatives of the gas temperature and density at that radius. The precise relationship is (discussed in FLG)

$$M(<r) = \frac{-kT_{gas}}{G\mu M_H}\left(\frac{d\log \rho_{gas}}{d\log r} + \frac{d\log T_{gas}}{d\log r}\right)r. \quad (1)$$

To determine M87's mass we must derive the density and temperature profiles of the gas from the X-ray data and understand the errors in this process. We are thus able to proceed without reference to any theoretical model for the origin or distribution of the X-ray emitting gas.

II. OBSERVATIONS

Most of the X-ray data that allow us to measure M87's mass have been obtained with the imaging proportional counter (IPC) aboard the *Einstein Observatory*. When placed at the focus of the *Einstein Observatory* X-ray mirror, the IPC forms images from X-rays in the 0.2–4.5 keV energy range with spatial resolution of 1.5 in each axis. The useful field of view is 60′ × 60′. The IPC also returns low-resolution spectral information, with $E/\Delta E \sim 1$. The IPC and other instruments aboard the *Einstein Observatory* are described in detail by Giacconi *et al.* (1979).
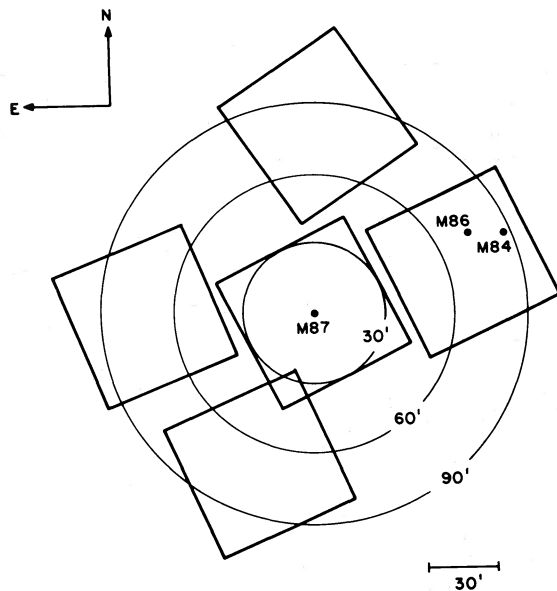

FIG. 1.—A schematic representation of the IPC fields used to study the X-ray emission in the M87 region. The optically derived Virgo Cluster center is located near M86 (Zwicky, Herzog, and Wild 1961).

The observations we describe in this paper consist of two fields centered on M87 (one with an aluminum filter in place) and four adjacent fields that provide reasonably complete azimuthal coverage to a radial distance of 90′ from M87. The locations of these fields are shown schematically in Figure 1. The pointing directions, exposure times, and observation dates of the six pointings are summarized in Table 1.

III. ANALYSIS

Our analysis of these data proceeds in two parts. First, we discuss the deconvolution of the surface brightness profile to obtain the density profile. Because of the fact that all the rates of radiative processes from ionized gas are proportional to the square of the density and the fact that the X-ray emissivity in the 0.3–4.0 keV band is relatively constant with temperature above 2 keV, this deconvolution may proceed without initial reference to the temperature profile of the gas. The errors in this assumption are discussed below. Second, we use the radially resolved IPC spectral data and the integrated spectrum of M87 as observed by previous instruments to constrain the temperature distribution in the gas.

a) Surface Brightness

To justify the analysis of the surface brightness data in radial rings, we examine a contour map for signs of asymmetry or ellipticity. Figure 2 is a 0.3–4.0 keV X-ray contour map of the central region of M87, corrected for background and vignetting, although both of these corrections are small. The contour map extends to a projected radius of ~ 15′; data at greater radii are distorted by the presence of the IPC window support structure. The outermost contour is slightly elliptical, with a ratio of major to minor axis of ~ 1.2. The limits on ellipticity derived from the fields adjacent to M87 are discussed below. We average through the small ellipticity in what follows.

All events having detected pulse heights falling in the nominal energy range 0.3–4.0 keV in each of the six fields were binned in annuli about the position of M87 ($12^h28^m18^s$, 12°40′). The width of each annulus was 1′ in the central field and 5′ for the four adjacent fields. Background due to the diffuse X-ray background, charged particles, and atmospheric X-rays produced from solar illumination has been estimated from long observations of fields containing only weak point sources. After screening the data and subtracting point sources, we find that the total background rate in the 0.3–4.0 keV energy band is constant within ± 15% from field to field. Background in each of the M87 fields has been determined from the long-exposure fields by binning the data in corresponding annuli from the same positions within the IPC.

TABLE 1

IPC OBSERVATIONS OF M87 REGION

| SEQUENCE NUMBER	COMMENTS	POINTING DIRECTION (1950)		EXPOSURE TIME (seconds)	DATES OBSERVED
		R.A.	Decl.		
10362	Centered on M87	$12^h28^m18^s$	12°40′	9121	1981 Jan 11
10361	Centered on M87, Al filter in	12 28 18	12 40	19035	1981 Jan 12, 13
281	North of M87	12 28 00	14 0	13843	1978 Dec 22, 23
278	West of M87	12 24 00	13 0	33834	1978 Dec 21, 22
279	South of M87	12 30 00	11 37.5	22420	1978 Dec 25, 26
4313	East of M87	12 33 06	12 40	8408	1979 Jul 1
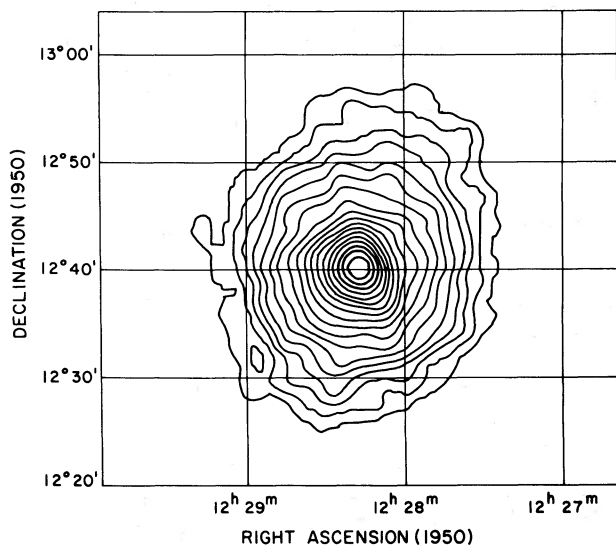
FIG. 2.—A 0.3–4.0 keV X-ray contour map made using data from the field centered on M87. Background has been subtracted, and a correction has been made for the vignetting of the telescope optics. The outermost contour is at a level of ~ 1.9×10^{-13} ergs cm^{-2} s^{-1} arcmin^{-2}, and the contour levels are separated by a factor of 1.2 in surface brightness. The data have been smoothed by convolution with a Gaussian function with $\sigma = 45''$. The outermost contour is slightly elliptical, with a ratio of major to minor axis of ≤ 1.2. For an assumed distance to M87 of 15 Mpc, 1′ corresponds to 4.4 kpc.

All point sources with count rates greater than 5×10^{-3} counts s^{-1} (~ 1.4×10^{-13} ergs cm^{-2} s^{-1}) in the 0.3–4.0 keV band were detected in both the M87 and background fields. To avoid biasing or contaminating the final surface brightness profiles, we rejected a region surrounding each source from the corresponding posi-

tion in both the M87 and background fields. Finally, the net (background subtracted) counts in each annulus were calculated. A systematic error of 20% of the background level subtracted in each annulus was added in quadrature to the statistical errors to allow for variations in the background level. Because ~ 50% of the background in this energy range is due to the diffuse X-ray background, this systematic error is sufficient to allow for diffuse X-ray background variations of 40%. Furthermore, the surface brightness of M87 (uncorrected for vignetting of the telescope optics) is ~ 4 times the background level at a radial distance of 30′ and approximately equal the background level at 70′. We are therefore confident that uncertainties in the background subtraction are included adequately in our errors.

The net surface brightness was next converted from counts s^{-1} arcmin^{-2} to ergs cm^{-2} s^{-1} arcmin^{-2} in the 0.2–4.0 keV energy band. A gas temperature of 3.5 keV at radii larger than 3′ (1.7 keV for smaller radii) and a hydrogen column density of 2.5×10^{20} cm^{-2} were assumed in this conversion. We calculated a conversion factor for each annulus independently, taking into account the local gain of the IPC and the vignetted effective area of the telescope. Only data within 30′ of the optical axis of the telescope were used, so that the maximum correction for vignetting is a factor of 2 at 1.5 keV and below.

In order to assess the errors in this process, including those due to uncorrected nonlinearities in the IPC spatial response, gain variations in the IPC, and vignetting correction inaccuracies, we applied the same procedure to data acquired during occultation by the sunlit Earth. The sunlit Earth is a strong source of scattered solar X-rays and provides, in essence, a flat field correction. The individual deviations of the vignetting- and gain-corrected data were compared with the average level,

and the 1 σ errors were found to be slightly under 6%. A constant error of 6% of the net vignetting-corrected surface brightness therefore was added in quadrature to the previous errors.

The final vignetting-corrected, background-subtracted surface brightness data are shown in Figure 3. The data beyond 30′ are averages of the surface brightness in the four adjacent fields. The error bars shown here include the statistical errors (which are quite small) and the systematic errors of background subtraction and vignetting/gain correction discussed above. We have considered an additional source of systematic error, X-ray photons that are scattered by the mirror instead of focused to a point. This tends to flatten the observed surface brightness profile, but simulations show that this effect is small in comparison to the previous sources of systematic error, so that a correction is not necessary.

An interesting point to note from Figure 3 is that at radii beyond 10′ the surface brightness profile appears to follow an approximately constant power-law dependence. This contrasts with the conclusion drawn by

FLG (on the basis of a single adjacent field instead of the average of four used here) that the surface brightness appeared to level out beyond about 60′. This is significant because there is no apparent way to differentiate between M87 gas and Virgo Cluster gas in the absence of a break in the surface brightness.

The surface brightness data were fit to an analytic function of the form $S(r) \propto [1 + (r/a)^2]^{-n}$ by searching for minimum χ^2. This functional form was introduced by Cavaliere and Fusco-Femiano (1976) to describe isothermal hydrostatic gas distributions in the gravitational field of an isothermal sphere. We use it here simply because it is a convenient analytic form that approaches $S \propto r^{-2n}$ for $r/a \gg 1$. Six different fits were performed: to each of the four adjacent fields independently, to the average of these fields, and to the complete data set, including the central field (without Al filter). The parameter core radius, a, was determined to be 1.62 ± 0.28 in the fits to the complete data set. The best fitting values of n are listed in Table 2. The errors correspond to the values where the χ^2 increases by 4.6 from the minimum value, corresponding to 90% confidence intervals (Avni 1976). The value of the core radius determined is useful for an empirical description of the surface brightness data, but it is not a meaningful measure of the core size due to two factors: the IPC point response of ~ 1.5 has not been deconvolved, and the small amount ($\leq 15\%$ of total counts at radii less than 5′) of nonthermal emission associated with the nucleus, the jet, and the radio lobes has not been subtracted (Schreier, Gorenstein, and Feigelson 1982).

We have also checked for asymmetry of the X-ray emission in the four fields surrounding M87. This has been done by finding the allowed normalization range for the nominal surface brightness model ($n = 0.81$) for each of the four fields, as summarized in Table 2. The numbers are consistent with radially symmetric surface brightness, but differences of up to $\sim 50\%$ are possible. When the power-law dependence is considered, a deviation of 50% in normalization corresponds to a radial scale change of $\sim 30\%$.

We note in passing here that the $\sim 15\%$ X-ray background variations reported by Lea *et al.* (1979) near the Virgo Cluster cannot be an additional significant source of error in our surface brightness analysis. Approximately half the background of the IPC in the 0.3–4.0 keV energy range is due to the X-ray background. Therefore, the 15% variations reported by Lea *et al.* would result in $\sim 8\%$ background variations in the IPC. This is well below the 20% systematic error we have allowed.
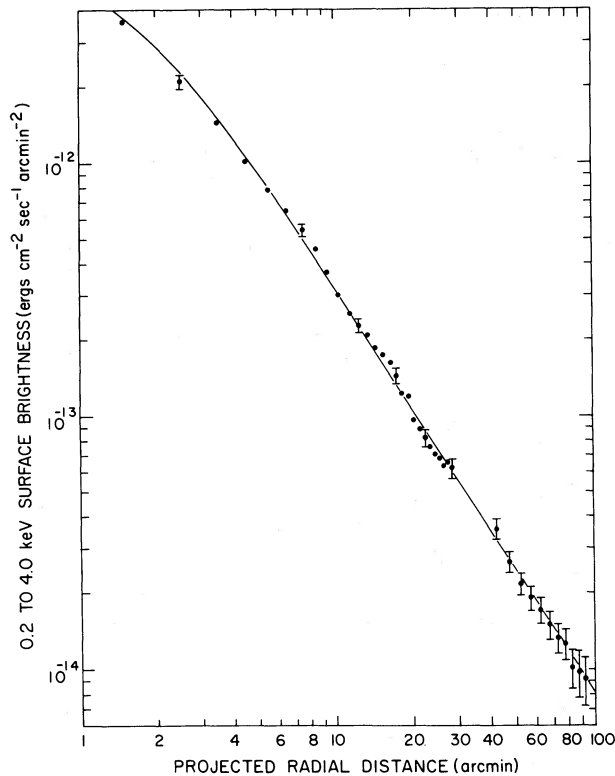

FIG. 3.—The 0.2–4.0 keV surface brightness profile of M87. Background has been subtracted, and a correction has been made for the vignetting of the telescope optics. The data within 30′ are from the field centered on M87. Beyond 30′, the average surface brightness of the four adjacent fields is shown. The curve indicates $S \propto [1 + (r/1.6)^2]^{-0.81}$. For a distance to M87 of 15 Mpc, 1′ corresponds to 4.4 kpc.

b) The Density Profile

The surface brightness profile can be deprojected to yield the density profile. The numerical form we have

TABLE 2

M87 SURFACE BRIGHTNESS PROFILE FITS AND THE DECONVOLVED DENSITY PROFILES

Data Set	Surface Brightness Index n[a]	Surface Brightness[b] Relative Normalization S_0	Density Index p[c]
N field	0.67 ± 0.23	5.0 ± 1.9	0.59 ± 0.12
S field	1.01 ± 0.22	7.0 ± 1.3	0.76 ± 0.11
W field	1.01 ± 0.50	6.7 ± 1.2	0.76 ± 0.25
E field	0.83 ± 0.25	5.1 ± 1.4	0.67 ± 0.13
Average of above adjacent fields ...	0.86 ± 0.14	6.1	0.68 ± 0.07
Complete data set	0.808 ± 0.024	...	0.654 ± 0.012

[a] From expression surface brightness $S = S_0[1 + (r/a)^2]^{-n}$.

[b] Range of acceptable normalizations for $n = 0.81$. The units are 10^{-12} ergs cm^{-2} s^{-1} arcmin^{-2} (0.2–4.0 keV).

[c] From deconvolved density, $\rho \propto [1 + (r/a)^2]^{-p}$, $p \equiv (n + 1/2)/2$.

chosen for the surface brightness profile corresponds to a density profile $\rho(r) \propto [1 + (r/a)^2]^{-p}$, where $p = (n + 1/2)/2$, if the gas is assumed to be isothermal. Thus, the values of n in Table 2 can be simply converted to yield the density distribution and its errors. The electron density normalization derived from the flux measurements is 4.2×10^{-2} cm^{-3}, if we take the distance to M87 to be 15 Mpc. The quantity required for the mass measurement is $d \log \rho / d \log r$ (see eq. [1]). For the density distribution considered here,

$$\frac{d \log \rho}{d \log r} = \frac{-2p(r/a)^2}{1 + (r/a)^2}.$$

The error in $d \log \rho / d \log r$ caused by the assumption of isothermality beyond 3' in the deconvolution is less than 5% in the radial range between 5' and 90' for the allowed temperature profiles described in § IIIe). This error has been determined by calculating the surface brightness profile (see also § IIIe) expected from the nominal density profile and the temperature profiles of models 3 and 4 below. The resultant surface brightness profile was then deconvolved isothermally, and the inferred density profile was compared with the actual input density distribution.

We have considered an additional source of error in the deconvolution of the surface brightness to yield the density profile, namely, the possibility that the abundance of heavy elements in the gas varies with radius. Due to the strong iron L shell line emission at the temperatures encountered in the gas surrounding M87, the density derived is dependent on the abundance of heavy elements. To assess the magnitude of this effect, the error in the derived density gradient has been calculated if an abundance change of a factor of 8 (200% of nominal to 25% of nominal) between radii of 3' and 100' were ignored. We find that such an abundance gradient

would create an error in the derived $d \log \rho / d \log r$ of magnitude 0.1, which is less than 10% of the value (nearly constant at 1.3) we observe.

c) *Spectral Fits*

Since the previous paper (FLG), the spectral response of the IPC has been recalibrated. Observations of other sources whose spectra are well known have been helpful in this regard. The spectral response of the IPC is now calibrated to an accuracy of 3%. By this, we mean that once the IPC gain is determined to sufficient accuracy, the number of counts in each of the IPC's 16 pulse-height channels can be predicted to better than 3% accuracy for a specified input spectrum. This error includes the effect of uncertainties in the effective area of the mirror/IPC combination, in the energy resolution of the IPC, and in the energies of the pulse-height channel boundaries. When the previous paper was written, the corresponding error exceeded 10% and forced FLG to a nonstandard renormalization procedure. This is no longer necessary.

The spectral fitting procedure used consists of four steps very similar to those in the surface brightness analysis: (1) Data from the M87 and background fields are binned in annuli, with positions near point sources rejected. The exposure-normalized background is subtracted, and 20% bin-by-bin systematic background subtraction errors are added. (2) The gain and distribution of gain variations within the annuli are determined from calibration data. (3) The appropriate effective areas for the annuli are calculated. (4) Finally, to allow for the systematic calibration errors discussed above, systematic errors of 3% of the net counts in each channel are added in quadrature to the statistical errors. At this point, model spectra may be folded through the instrumental response and compared with the data using the χ^2 test.

i) *IPC Calibration Verification*

The identical procedure was tested on nine clusters observed by the IPC that had previously measured X-ray spectra. Most of these clusters had been observed in the 2–10 keV band by proportional counters aboard the *OSO 8* and *HEAO 1* satellites (Mushotzky *et al.* 1978; Mushotzky 1982). The IPC observations spanned the complete range of gains experienced in flight by the IPC. The previously measured cluster temperatures encompassed the range from 2–8 keV and were derived using a thermal bremsstrahlung plus Gaunt factor model. This model neglects the line emission from heavy elements that is known to be present, but the strongest lines are due to the iron L complex that falls below 1.5 keV, so this was not a significant source of error above 2 keV. The IPC temperatures were derived by fitting detailed thermal models, including line emission, because the IPC temperatures are measured in the 0.2–4.5 keV energy range, where line emission is important. The thermal models were obtained from the code of Raymond and Smith (1977, 1982) for the calculation of X-ray emission from an optically thin plasma. The nominal cosmic abundance of heavy elements was assumed (Allen 1973), with the iron abundance, which is the most important, at 4.0×10^{-5} relative to hydrogen by number.

The temperature ranges (and hydrogen column densities) allowed by the IPC data were determined by searching for minimum χ^2, and the χ^2 minimum plus 4.6 limits (nominally 90% confidence for two parameters). In eight out of the nine cases, the measured IPC temperature limits overlapped the previous measurements. In the ninth case, the cluster A2147, the previous measurements indicated a multicomponent spectrum. The IPC measurement of kT greater than 3.5 keV is higher than the dominant low-temperature component. Even if this is regarded as a discrepancy, the agreement in the other eight cases indicates that the empirical IPC error limits correspond well to the nominal 90% confidence limits. We are therefore able to proceed to the analysis of the IPC M87 spectral data with confidence in the instrumental calibration.

ii) *Fits to the M87 Data*

The data were binned in six radial bins, 0′–3′, 3′–6′, 6′–9′, 9′–12′, 12′–15′, and 21′–27′. The region from 15′ to 21′ is heavily shadowed by the IPC window support structure, so this region was excluded from the analysis to avoid systematic effects arising from an energy-dependent term in the shadowing.

The interpretation of these spectral data is complicated by the fact that the gas distribution is seen in projection, and the temperature measured at a given projected radius really corresponds to the emission-weighted temperature of the gas integrated along the line of sight. This effect is less important than one might guess, because the emission is weighted by the square of the gas density, which approximately follows an $r^{-2.6}$ dependence, but nevertheless, it must be taken into account. This can be done by taking a proposed density and temperature profile, calculating the emission at each position of constant projected radius, and integrating the total emission along the line of sight. The resultant integrated spectrum may then be convolved with the IPC spectral response and compared with the data by means of the χ^2 test. However, as a guide to possible temperature gradients, we first fit data in each of the six radial bins with isothermal spectra calculated from the Raymond and Smith code (1977, 1982). The results are shown in Figure 4. The error bars correspond to ~ 90% confidence (χ^2 minimum plus 4.6) limits. The interstellar absorption was allowed to vary freely and falls in the range $2–4 \times 10^{20}$, consistent with previous X-ray results (Fabricant *et al.* 1978; Lea *et al.* 1979) and H I measurements (Heiles 1975). Also plotted in Figure 4 are the results from the solid state spectrometer (SSS) data described by Lea, Mushotzky, and Holt (1982). The SSS data have also been analyzed using the thermal models of Raymond and Smith. The iron abundance assumed in the derivation of the temperatures from the SSS data is 80% of the iron abundance we have assumed. The derived temperatures would have been $\leq 10\%$ higher had they used the same iron abundance (Mushotzky 1982). For the 0–3′ bin, the temperature plotted from the SSS data is that of the dominant thermal component. The 0′–3′ SSS data also indicate the presence of emission from lower temperature gas and an absorbed power-law component, presumably associated with nonthermal emission from the nuclear region. This region has been studied by Canizares *et al.* (1982), who present a detailed analysis of the data from the *Einstein Observatory* focal plane crystal spectrometer observations of M87. Since we are concerned with the bulk of the mass, which resides at considerably larger distances, the complexities of the spectrum at radii less than 3′ are not relevant to our discussion. The emission measure of the gas at temperatures below ~ 1.5 keV is well below (by more than an order of magnitude) the integrated emission measure of the whole region. In the following analysis, we confine ourselves to the spectral data beyond 3′.

The IPC and SSS results agree quite well. One notes that the SSS error bars for the point at 7′ off axis are as large as those from the IPC even though the SSS energy resolution is an order of magnitude better. This is perhaps explained by the fact that the IPC has much lower internal background than the SSS and, hence, a superior signal-to-noise ratio. In addition, because the IPC is able to observe a complete annulus (264 square arcmin between 4′ and 10′), while the SSS has a fixed 28 square arcmin field of view, the IPC collects many more pho-
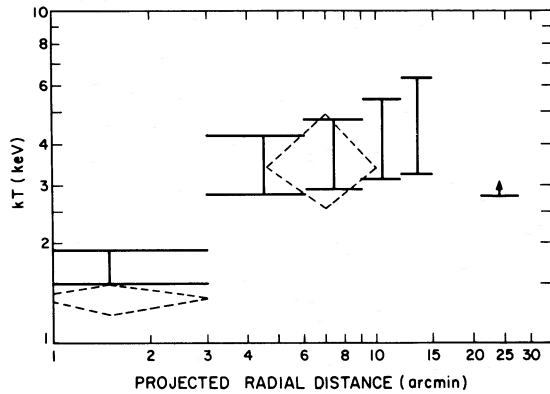
FIG. 4.—The temperatures (and errors) derived by isothermal fits of Raymond and Smith (1977, 1982) thermal spectra to the IPC radially binned spectral data are shown as solid lines. No correction has been made for projection effects. Data from the solid state spectrometer (Lea, Mushotzky, and Holt 1982) are shown for comparison (*dashed diamonds*).

tons in an observation of equal length. At any rate, the agreement gives further confidence in the IPC spectral calibration.

An independent partial confirmation of the spectral results is possible by comparison of the spatially re-solved IPC count rates with and without the aluminum filter in place. Because the Al filter absorbs incident X-rays at energies below ~ 0.8 keV, a lower limit for the temperature can be derived from the ratio of these count rates. This result is not dependent on the details of the IPC spectral response. We find that the projected tem-perature must exceed 1.3 keV for both the 0'–3' (ratio 0.146 ± 0.003 in the 0.3–4.0 keV pulse-height bins) and 3'–6' (ratio 0.139 ± 0.004) bands, in agreement with the results discussed above.

We are unable to measure the temperature of the gas beyond ~ 25' even though we are able to follow the surface brightness profile to ~ 90'. The measurement of temperature requires a much higher signal-to-noise ratio than that needed to measure the surface brightness in a broad band. The main limitation in the present case is due to systematic errors in the background subtraction.

iii) *Sources of Error in the Spectral Fits*

We have investigated two sources of systematic error in our temperature measurements and have discounted a third. The first, basically theoretical in origin, is the accuracy of the thermal models we have used to inter-pret the IPC spectral data. There are acknowledged uncertainties in the atomic physics data and calcula-tions used to predict the X-ray spectra emitted by a hot plasma. Furthermore, there may be abundance gradients in the gas as discussed previously, and the abundance (if constant) may be different from that which we have assumed. In order to understand how sensitively

our conclusions depend on these factors, we have com-pared the temperatures obtained using two different X-ray emission codes: the Raymond and Smith code mentioned previously and the code of Mewe and Gronenschild (1981). These two programs begin with somewhat different atomic physics assumptions, particu-larly for iron, where the data are most incomplete.

We fit the spectral data in two of the radial bins (3'–6' and 12'–15') with isothermal model spectra at a variety of abundances. Using the Raymond and Smith calculations, we compared the results of varying the abundance of all elements heavier than H by a factor of 2 above and below the Allen (1973) values. With the Mewe and Gronenschild code, we studied the effect of varying the Mg, Si, S, Ca, Fe, and Ni abundances by a factor of 5 relative to the other elements about the Allen values. The temperatures derived in these fits (90% confidence) are shown in Table 3. We draw three con-clusions: (1) With the Allen abundances, the tempera-tures derived using the Mewe and Gronenschild code are 20% lower than those obtained with the Raymond and Smith code. Since we have used the Raymond and Smith models in what follows (§ IIIe), the Mewe and Gronenschild models would lead to M87 masses up to 20% lower. (2) The temperature uncertainty expressed as a percentage of the derived temperature at a fixed abundance is similar for the two models. (3) The varia-

TABLE 3

ALLOWED TEMPERATURE RANGES[a] FOR TWO SPECTRAL MODELS WITH VARIOUS HEAVY-ELEMENT ABUNDANCES

A. RAYMOND AND SMITH THERMAL MODELS

	kT FROM ANNULUS[c]	
ABUNDANCE[b]	3'–6'	12'–15'
50%	2.5–3.8 keV	2.9–5.7 keV
100%	2.8–4.2 keV	3.2–6.2 keV
200%	3.2–4.6 keV	3.7–6.6 keV
Total range (50%–200%) ...	2.5–4.6 keV	2.9–6.6 keV

B. MEWE AND GRONENSCHILD THERMAL MODELS

	kT FROM ANNULUS[c]	
ABUNDANCE[d]	3'–6'	12'–15'
20%	1.9–3.1 keV	2.2–5.8 keV
100%	2.1–3.3 keV	2.2–5.3 keV
500%	2.3–3.6 keV	2.2–5.3 keV
Total range (20%–500%) ...	1.9–3.6 keV	2.2–5.8 keV

[a] 90% confidence intervals from χ^2 fits.
[b] 100% from Allen 1973. All elements except H scaled by stated factor.
[c] Results of fits to isothermal models.
[d] 100% from Allen 1973. Mg, Si, S, Ca, Fe, Ni scaled by stated factor.

tion of the temperature derived as the assumed abundance is changed is small in both cases. At most, the upper and lower temperature limits change by only ~ 10%. These three results allow us to conclude that our mass measurements are not sensitively dependent on the abundance of heavy elements or the details of the atomic physics calculations.

The second source of systematic error considered is the effect of internal scattering by the X-ray mirror. Since scattering is more pronounced at high energies, and the surface brightness falls with radius, scattering systematically tends to harden spectra at large radii and soften spectra at small radii; however, the effect is rather small. Prior to launch, scattering profiles had been measured at several X-ray energies. A detailed simulation with a 3 keV isothermal input model with the surface brightness distribution of M87 showed a small positive temperature gradient after scattering was considered. The spectrum after scattering was compared with the input spectrum in 10 bins, each of width 3'. The maximum deviation from the isothermal input spectrum was only 10% at the radial extremes of 0'–3' and 27'–30'. We judged this to be insignificant, and furthermore, any correction for this effect would only slightly increase our lower limits on the mass of M87.

A third possible source of error, suggested by Binney and Cowie (1981), is that the cooling flow taking place in the central few arcminutes of M87 may significantly alter the ionization balance of the gas, leading to errors in the temperature measurements. This question has been considered in detail by Canizares et al. (1982) and Lea, Mushotzky, and Holt (1982), but they have found departures from ionization equilibrium to be negligible. Since the recombination time of the cooling gas is an order of magnitude shorter than the cooling time, such effects are not expected.

d) Constraints on the Allowed Temperature Gradients

The remaining problem in the analysis of the spectral data is to calculate limits on the temperature gradient in M87. In contrast to the previous paper (FLG), in which the thrust of the analysis was to calculate the minimum mass within 50' of M87, our objective here is to explore the range of possible values of the mass at smaller radii as well. In particular, we wish to examine the suggestion of Binney and Cowie (1981) that M87 is a low-mass galaxy surrounded by a pressure-confined atmosphere of cooling gas. Their analysis is based on two premises: that the temperature of the hot gas surrounding M87 has an approximately constant large positive gradient ($d \log T / d \log r \sim +0.7$) and that this gas is contained by 8 keV gas filling the Virgo Cluster. This large positive temperature gradient cancels the effect of the negative density gradient in equation (1), leading to lower masses than those calculated by FLG at radii less than ~ 30'.

Binney and Cowie have obtained a mass comparable to or larger than that calculated by FLG beyond ~ 50', but they assign this mass to the Virgo Cluster, not M87.

We require all models for the temperature gradient to be consistent with two simultaneous spectral constraints. The first of these is the five bins (beyond 3') of IPC spectral data discussed above. The second is the integrated spectrum from the M87 region measured in the energy range 2–10 keV by wide field-of-view proportional counters aboard four previous satellites, *Uhuru*, *Ariel 5*, *OSO 8*, and *HEAO 1* (Kellogg, Baldwin, and Koch 1975; Mitchell, Ives, and Culhane 1977; Mushotzky et al. 1978; Lea et al. 1981). The integrated temperatures and fluxes measured by these instruments are summarized in Table 4, together with their fields of view. Also shown are the IPC fluxes in the 0.2–4 keV range and the fluxes extrapolated to the 2–6 keV range for comparison. The nominal IPC fluxes in both energy ranges are based on an assumed Raymond and Smith thermal spectrum with $kT = 3.5$ keV and $N_H = 2.5 \times 10^{20}$. The lower and upper limits correspond to assumed spectra of $kT = 2.0$ keV and $N_H = 1.0 \times 10^{20}$ and $kT = 5.0$ keV and $N_H = 4.0 \times 10^{20}$, respectively. The extrapolated 2–6 keV IPC fluxes are consistent with the interpretation that the IPC sees all the emission within a limit of 100' that was detected by previous instruments with much larger fields of view. The previous fluxes are in close agreement. However, the errors are large enough so that as much as 25% of the emission seen by the wide field-of-view instruments could lie outside the IPC's field of view. Of course, this excess gas could be cooler, hotter, or the same temperature as the emission-weighted temperature of the gas within 100'. Our principal objective is to find the lower limits on the mass of M87, i.e., an upper limit to a positive temperature gradient. If the temperature of the gas exterior to 100' is cooler than the emission-weighted temperature within 100', the temperature gradient is not positive. If these gas temperatures are the same, it is valid to use the spectrum seen by the wide field-of-view instruments to constrain the integrated spectrum within 100'. Finally, if the gas exterior to 100' is hotter than the interior weighted temperature, the use of the wide field-of-view temperatures is conservative.

Reports by Davidson (1978) and Lawrence (1978) that a hard spectral component ($kT \gtrsim 8$ keV) from the Virgo Cluster region was probably associated with Virgo Cluster emission have been placed in strong doubt by recent work (Lea et al. 1981; Lea, Mushotzky, and Holt 1982). This hard spectral component has a power-law spectral shape and is probably due to nonthermal emission from the nucleus of M87. Only approximately 6% of the integrated 2–6 keV flux from M87 is provided by the hard component, although it dominates the spectrum above 15 keV. Two of the temperatures listed in Table 4 (*OSO 8* and *HEAO 1* A-2) have been de-

TABLE 4

M87 X-Ray Fluxes and Integrated Temperatures

A. IPC M87 Fluxes[a] (ergs cm^{-2} s^{-1})

Radial Band	0.2–4.0 keV	Extrapolated 2.0–6.0 keV
0′–50′	$7.4 \pm 1.1 \times 10^{-10}$	$3.3^{+0.6}_{-1.1} \times 10^{-10}$
0′–100′	$1.0 \pm 0.16 \times 10^{-9}$	$4.4^{+0.9}_{-1.5} \times 10^{-10}$

B. Other Instruments

Satellite	2.0–6.0 keV Fluxes	kT (keV)	Field of View (FWHM)
OSO 8	3.8×10^{-10}	2.2 ± 0.2	5°
Ariel 5	3.7×10^{-10}	2.8 ± 0.3	3°5×3°5
Uhuru	3.7×10^{-10}	2.6 ± 0.1	5°×5°
HEAO 1 A-2	...	2.0 ± 0.2	1°5×3°
Average of above four	3.7×10^{-10}	2.4	...

[a] Errors in the IPC fluxes are dominated by uncertainties in the integrated temperature (see text).

termined using two-component fits, including a power-law hard component, but the *Uhuru* and *Ariel 5* results are single-temperature thermal bremsstrahlung fits in the energy range above 2 keV. This probably accounts for the slightly higher *Uhuru* and *Ariel 5* temperatures. The average of the four measurements is 2.4 keV. If the 8 keV gas is indeed absent, the model described by Binney and Cowie (1981) is untenable.

In order to test various models for the temperature gradient, a computer program was written to calculate the resultant X-ray spectra, based on the work of Raymond and Smith (1977, 1982). This program, given a radial temperature and density profile, calculates the emission (with 20 eV energy resolution) in small cells along the line of sight. The cells within specified limits of projected radius are integrated along the line of sight, and the resultant spectra are saved for comparison (after convolution with the IPC spectral response) with the IPC data.

In addition, the integrated spectrum over a large region, here taken to be within a projected radius of 100′, is calculated. Because we do not have direct access to the raw data from the wide field-of-view instruments, this integrated spectrum is handled differently. The 2–6 keV spectrum is added up into 20 bins, each 200 eV wide, and compared directly with isothermal spectra binned the same way. The isothermal temperature giving the minimum least squares deviation from the integrated spectrum is found. We require that the model under consideration be consistent with the IPC data in each of the five radial bins beyond 3′ at least at the 5% probability level (based on the χ^2 test), and that the isothermal temperature best fitting the integrated spectrum (0′–100′)

fall in the range 1.5–4.0 keV. We have adopted the rather conservative upper limit of 4 keV in the 2–6 keV energy range to render our analysis independent of the origin of the hard spectral component. We assume the Allen abundances and take $\rho(r) \propto [1 + (r/a)^2]^{-0.65}$.

e) Temperature Gradient Results

Although there are, in principle, an infinite variety of possibilities for the temperature distribution of the X-ray emitting gas, we have considered two classes of models that we believe map out the lower and upper limits of M87's mass at radii beyond 5′. We make no attempt to measure the mass at smaller radii for the reasons discussed in § IIIc). The first class, in which the temperature gradient is constant with radius beyond ∼ 3′, includes the model of Binney and Cowie (1981), but we have allowed both positive and negative temperature gradients. The second class consists of models in which the temperature gradient is constant (and positive) until a given radius beyond which the temperature is constant. The abrupt change in gradient is perhaps unphysical, but we consider these models because they provide a firm lower limit on the mass at radii less than 20′.

In each of these two classes of models, the absolute temperature normalization of the model considered was adjusted for each gradient under consideration to bring it into as close agreement as possible with the spectral data. We find that the steepest constant positive gradient has $d \log T/d \log r = 0.3$, and the steepest constant negative gradient has $d \log T/d \log r = -0.4$.

As a comparison, the better fitting of the two limiting models described by Binney and Cowie (1981) failed to
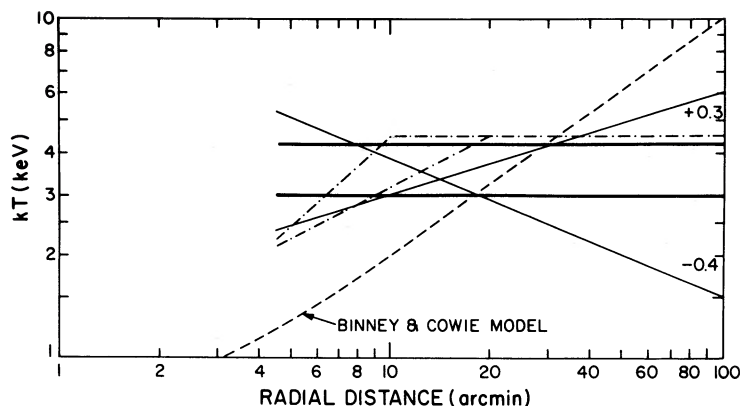
FIG. 5.—The temperature profiles plotted are consistent with the available spectral data, except the one shown as a dashed line, which corresponds to the model of Binney and Cowie (1981). These profiles have been derived allowing for projection effects, and the radii plotted refer to a spherical coordinate system.

be consistent with any of the IPC radial bins except the 21'–27' bin. The probability of obtaining the χ^2 values calculated for the 3'–6', 6'–9', 9'–12', and 12'–15' radial bins by chance are < 0.1%, < 0.1%, < 1%, and ~ 1.5%, respectively. The best fitting temperature for the integrated 2–6 keV emission in the Binney and Cowie model is 4.7 keV, which is higher than the conservative 4 keV limit derived from the observations. This model has $d \log T/d \log r \sim +0.7$. Furthermore, Canizares et al. (1982) reported that the large quantities of cooling gas at temperatures near 1 keV present at small radii in the Binney and Cowie models are ruled out by the limits on Fe xx emission.

The steepest possible temperature gradients for models in which the temperature gradient is constant until a radial limit is reached are $d \log T/d \log r = +0.9$ and +0.5 for radial limits of 10' and 20', respectively. We did not consider models with larger limiting radii since these would result in M87 masses indistinguishable from the constant $d \log T/d \log r = 0.3$ model.

These allowed temperature profiles are shown in Figure 5. The radii plotted in Figure 5 refer to a spherical coordinate system and are not projected radii. The Binney and Cowie model, which is inconsistent with the spectral data, is shown as a dashed line for comparison. The isothermal temperature limits are also plotted.

f) The Allowed Mass Ranges

The density profile ($d \log \rho/d \log r$), the gas temperature, and the gas temperature profile ($d \log T/d \log r$) have now all been constrained at radial distances from 5' to 90' from M87. The results for the total interior mass at specified radii (calculated from eq. [1]) are summarized in Table 5 for each of the temperature gradient models considered. Also shown in Table 5 are the gas mass, the optical (V band) luminosity (from Oemler 1976, and de Vaucouleurs and Nieto 1978), and

the minimum mass-to-light ratio as a function of radius. The envelope of lower and upper mass limits as a function of radius is plotted in Figure 6, together with the optical mass measurements of Sargent et al. (1978), which extend only to ~ 1'. The error bars for the optical measurements have been calculated taking only the error in the velocity dispersion measurements into account; the true errors for the optical mass measurements will be somewhat larger.

It is appropriate to consider at this point the worst case systematic uncertainties in the normalization and radial dependence of the mass distribution plotted in Figure 6. These are due to possible abundance gradients, errors in the density deconvolution, and uncertainties in the models predicting the X-ray emission from a hot plasma, all discussed previously. We find that if all the uncertainties were to sum in a given direction, $d \log \rho/d \log r$ and $d \log T/d \log r$ could each change by 0.17, and the temperature normalization could change by 30%. Inserting these factors into equation (1), we find they correspond to mass normalization changes of a factor of 2. However, the functional dependence of the mass with radius is only slightly affected by these errors. By referring to equation (1) again, we see that power-law models for the temperature profile lead to power-law mass distributions if $d \log \rho/d \log r$ is approximately constant. If the systematic uncertainties under discussion are neglected, $d \log T/d \log r$ lies between +0.3 and −0.4, giving an M87 mass that varies as r^b, where b is in the range 0.6–1.3. The range of b is increased only slightly to 0.4–1.5 if the worst case systematic errors are added. The systematic uncertainties summarized in this paragraph are not explicitly included in Figure 6 because we feel that the worst case discussed here is relatively improbable.

Considered together, the X-ray and optical measurements indicate that the integral mass-to-light ratio (in solar units) must rise from the 5–15 range at 1' (or ~ 4

TABLE 5

M87 TOTAL INTERIOR MASS AND GAS MASS

Radius[a] (spherical coordinates)	Gas Mass[b] M	$\left(\dfrac{d \log \rho}{d \log r}\right)^c$	Solar[d] Luminosities	Mass $M_\odot$ Model 1	Mass $M_\odot$ Model 2	Mass $M_\odot$ Model 3	Mass $M_\odot$ Model 4	Mass $M_\odot$ Model 5	Mass $M_\odot$ Model 6	$M_\odot/L_\odot$
5′ (22 kpc)	...	−1.2	4.7×10^{10}	2.9×10^{12}	4.2×10^{12}	1.8×10^{12}	6.7×10^{12}	5.9×10^{11}	1.3×10^{12}	> 12
10′ (44 kpc)	6.2×10^{10}	−1.3	5.8×10^{10}	6.4×10^{12}	9.1×10^{12}	3.3×10^{12}	1.1×10^{13}	3.0×10^{12}	4.1×10^{12}	> 50
20′ (87 kpc)	2.1×10^{11}	−1.3	6.6×10^{10}	1.3×10^{13}	1.8×10^{13}	1.2×10^{13}	1.6×10^{13}	1.9×10^{13}	1.2×10^{13}	> 180
30′ (131 kpc)	4.3×10^{11}	−1.3	N.A.[e]	1.9×10^{13}	2.7×10^{13}	2.0×10^{13}	2.1×10^{13}	2.8×10^{13}	2.8×10^{13}	...
40′ (174 kpc)	7.0×10^{11}	−1.3	N.A.	2.5×10^{13}	3.6×10^{13}	2.9×10^{13}	2.4×10^{13}	3.8×10^{13}	3.8×10^{13}	...
50′ (218 kpc)	1.0×10^{12}	−1.3	N.A.	3.2×10^{13}	4.5×10^{13}	3.9×10^{13}	2.8×10^{13}	4.7×10^{13}	4.7×10^{13}	...
70′ (305 kpc)	1.8×10^{12}	−1.3	N.A.	4.4×10^{13}	6.3×10^{13}	6.1×10^{13}	3.4×10^{13}	6.6×10^{13}	6.6×10^{13}	...
90′ (392 kpc)	2.8×10^{12}	−1.3	N.A.	5.7×10^{13}	8.1×10^{13}	8.4×10^{13}	4.0×10^{13}	8.5×10^{13}	8.5×10^{13}	...

NOTE.—Model 1:   Isothermal 3.0 keV.
           Model 2:   Isothermal 4.3 keV.
           Model 3: $T(r) = 1.5\, r^{0.3}$ keV, r in arcmin.
           Model 4: $T(r) = 9.7\, r^{-0.4}$ keV, r in arcmin.
           Model 5: $T(r) = 0.57\, r^{0.9}$ keV for $r < 10'$, $T(r) = 4.5$ keV for $r > 10'$.
           Model 6: $T(r) = 1.0\, r^{0.5}$ keV for $r < 20'$, $T(r) = 4.5$ keV for $r > 20'$.

[a] M87's distance taken to be 15 Mpc. $1' = 4.36$ kpc, 100 kpc $= 23'$.

[b] These gas masses have been derived assuming the abundances of Allen 1973. If the mean abundance is a factor of 2 lower or higher, the derived masses are 12% higher or 16% lower, respectively.

[c] Estimated errors are $\leq 10\%$.

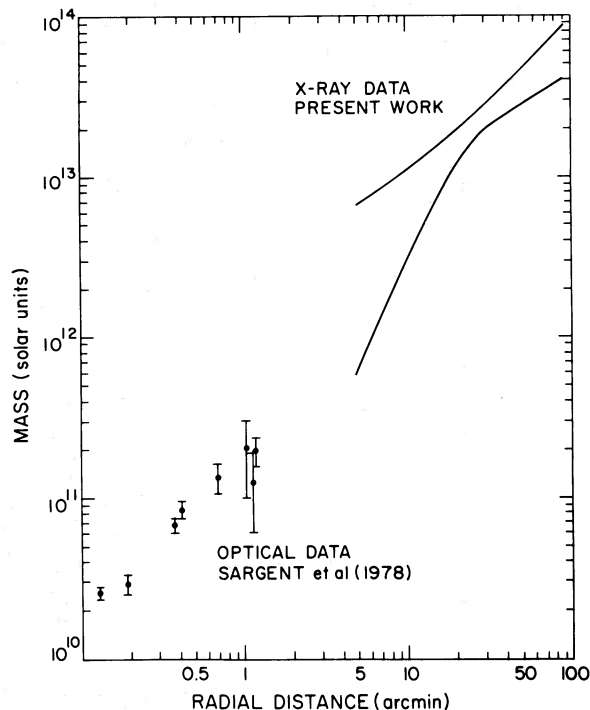[d] From Oemler 1976; de Vaucouleurs and Nieto 1978.

[e] N.A. = Not available.

FIG. 6.—The mass of M87 as a function of radius, summarizing both optical and X-ray results. The optical mass measurements extend to ~ 1′, and are derived from velocity dispersion measurements (Sargent et al. 1978). The allowed mass range derived from the present X-ray data is bounded by two solid lines. The exact radial mass dependence for each of the six temperature profiles considered is summarized in Table 5.

kpc) to over 50 at 10′ (~ 44 kpc) and over 180 at 20′ (~ 87 kpc). The X-ray emitting gas provides only ~ 5% of the dark matter that must be present. We believe that these results are free of assumption beyond the initial two of hydrostatic equilibrium and spherical symmetry. We note that the allowed mass range shown in Figure 6 at radii smaller than ~ 20′ (or 87 kpc) is larger than that shown in the previous paper (FLG).

IV. DISCUSSION

The fact that the mass we measure, at least at radii less than ~ 60′ (or ~ 260 kpc), is associated with M87 itself and not with a collection of other galaxies surrounding M87 can be established by referring to the Zwicky catalog of galaxies (Zwicky, Herzog, and Wild 1961). The number of galaxies brighter than 15th magnitude (1.5% of M87's optical luminosity) within projected radii of 30′, 60′, and 90′ of M87 are 3, 13, and 36, respectively. Of course, most of these are foreground and background objects. We have calculated the appropriate projection correction assuming a galaxy core radius of 2°. After applying this correction, we find 0.5, 4, and 15 galaxies lie within radii (spherical coordinates) of 30′, 60′, and 90′. Because there are so few bright galaxies near M87, it does not appear appropriate to assign the 3.1–5.6×10^{13} $M_\odot$ we observe within a radius of 60′ to a collection of galaxies rather than to M87.

The minimum mass-to-light ratio of the matter at radii between 10′ and 20′ (44–87 kpc) is 600 in solar units. This is comparable to the values inferred from H I

rotation curves at radii of ~ 30 kpc in M31 by Roberts and Whitehurst (1975). However, our results differ from those typically obtained with spiral galaxy rotation curves in that they extend to well beyond 250 kpc. At this radius, the total mass of dark matter is well over an order of magnitude more than the mass calculated by assuming a constant mass-to-light ratio of 5–10.

The question remains whether the formation of the massive dark halo that surrounds M87 is a result of its position near the center of the Virgo Cluster and the fact that it may lie nearly at rest with respect to the cluster. The implications of M87's great mass are obviously more profound if this is not the case. At the present time, the answer to this question is not clear. It is true that no other galaxies in the Virgo Cluster exceed ~ 2% of M87's X-ray luminosity (Forman 1982). However,

this may imply either that these galaxies do not have massive halos or simply that insufficient quantities of gas have collected to illuminate their halos in X-rays. Because the X-ray emission is proportional to the square of the gas density, a galaxy would only have 2% of M87's X-ray emission if it had ~ 14% of M87's gas mass. The type of study we have performed here would be impossible at present for a galaxy substantially less luminous in X-rays than M87.

REFERENCES

Allen, C. W. 1973, *Astrophysical Quantities* (3d ed.; London: Athlone), p. 208.
Avni, Y. 1976, *Ap. J.*, **210**, 642.
Bahcall, J., and Sarazin, C. 1977, *Ap. J. (Letters)*, **213**, L99.
Binney, J., and Cowie, L. L. 1981, *Ap. J.*, **247**, 464.
Canizares, C. R., Clark, G. W., Jernigan, J. G., and Markert, T. H. 1982, *Ap. J.*, **262**, 33.
Cavaliere, A., and Fusco-Femiano, R. 1976, *Astr. Ap.*, **49**, 137.
Davidson, P. J. N. 1978, *M.N.R.A.S.*, **183**, 39 p.
de Vaucouleurs, G., and Nieto, J. L. 1978, *Ap. J.*, **220**, 449.
Fabricant, D., Lecar, M., and Gorenstein, P. 1980, *Ap. J.*, **241**, 552 (FLG).
Fabricant, D., Topka, K., Harnden, F. R., Jr., and Gorenstein, P. 1978, *Ap. J. (Letters)*, **226**, L107.
Forman, W. 1982, private communication.
Giacconi, R., *et al.* 1979, *Ap. J.*, **230**, 540.
Heiles, C. 1975, *Astr. Ap. Suppl.*, **20**, 37.
Kellogg, E., Baldwin, J. R., and Koch, D. 1975, *Ap. J.*, **199**, 299.
Lawrence, A. 1978, *M.N.R.A.S.*, **185**, 423.
Lea, S. M., Mason, K. O., Reichert, G., Charles, P. A., and Reigler, G. 1979, *Ap. J. (Letters)*, **227**, L67.
Lea, S. M., Mushotzky, R., and Holt, S. S. 1982, *Ap. J.*, **262**, 24.

Lea, S. M., Reichert, G., Mushotzky, R., Baity, W. A., Gruber, D. E., Rothschild, R., and Primini, F. A. 1981, *Ap. J.*, **246**, 369.
Mathews, W. G. 1978, *Ap. J.*, **219**, 413.
Mewe, R., and Gronenschild, E. H. B. M. 1981, *Astr. Ap. Suppl.*, **45**, 11.
Mitchell, R. J., Ives, J. C., and Culhane, J. L. 1977, *M.N.R.A.S.*, **181**, 25p.
Mushotzky, R. F. 1982, private communication.
Mushotzky, R. F., Serlemitsos, P. J., Smith, B. W., Boldt, E. A., and Holt, S. S. 1978, *Ap. J.*, **225**, 21.
Oemler, A., Jr. 1976, *Ap. J.*, **209**, 693.
Raymond, J. C., and Smith, B. W. 1977, *Ap. J. Suppl.*, **35**, 419.
———. 1982, private communication.
Roberts, M. S., and Whitehurst, R. N. 1975, *Ap. J.*, **201**, 327.
Sargent, W. L. W., Young, P. J., Boksenberg, A., Shortridge, K., Lynds, C. R., and Hartwick, F. D. A. 1978, *Ap. J.*, **221**, 731.
Schreier, E., Gorenstein, P., and Feigelson, E. 1982, *Ap. J.*, **261**, 42.
Takahara, M., and Takahara, F. 1981, *Progr. Theor. Phys.*, **65**, 369.
Zwicky, F., Herzog, E., and Wild, P. 1961, *Catalogue of Galaxies and Clusters of Galaxies* (Pasadena: California Institute of Technology), p. 260.

D. FABRICANT and P. GORENSTEIN: Harvard-Smithsonian Center for Astrophysics, 60 Garden Street, Cambridge, MA 02138